

# **A High Lift Micro-Aerial-Robot Powered by Low Voltage and Long Endurance Dielectric Elastomer Actuators**

*Zhijian Ren<sup>†</sup>, Suhan Kim<sup>†</sup>, Xiang Ji, Weikun Zhu, Farnaz Niroui, Jing Kong, and Yufeng Chen\**

<sup>†</sup> Z. Ren and S. Kim contributed equally.

Z. Ren, S. Kim, Dr. X. Ji, Prof. F. Niroui, Prof. J. Kong, Prof. Y. Chen  
Department of Electrical Engineering and Computer Science  
Massachusetts Institute of Technology  
77 Massachusetts Avenue, Cambridge, MA, 02139, USA  
E-mail: yufengc@mit.edu

W. Zhu  
Department of Chemical Engineering  
Massachusetts Institute of Technology  
77 Massachusetts Avenue, Cambridge, MA, 02139, USA

**Keywords:** dielectric elastomer actuator, soft robotics, flapping-wing, micro-aerial-vehicles

## **Abstract**

Dielectric elastomer actuators (DEAs) are a special class of artificial muscles that have been used to construct animal-like soft robotic systems. However, compared with the state-of-the-art rigid actuators such as piezoelectric bimorphs and electromagnetic motors, most DEAs require higher driving voltages, and their power density and lifetime remain substantially lower. These limitations pose significant challenges for developing agile and power autonomous soft robots. Here, a low voltage, high endurance, and power-dense DEA based on novel multiple-layering techniques and electrode material optimization, is reported. When operated at 400 Hz, the 143 mg DEA generates forces of 0.36 N and displacements of 1.15 mm. This DEA is incorporated into an aerial robot to demonstrate high performance. The robot achieves a high lift-to-weight ratio of 3.7, low hovering voltage of 500 V, and a long lifetime that exceeds 2 million actuation cycles. With 20 seconds of hovering time, and position and attitude error smaller than 2.5 cm and 2°, the robot demonstrates the longest and best performing flight among existing sub-gram aerial robots. This important milestone demonstrates that soft robots can outperform the state-of-the-art rigid counterparts, and it provides an important step towards realizing power autonomy in soft robotic flights.

## 1. Introduction

Developing muscle-like actuators that enable agile, controllable, and robust robot locomotion is a major challenge in soft robotics. Among existing soft actuators, pneumatic<sup>[1]</sup> and hydraulic<sup>[2]</sup> actuators are most widely used because they are easy to fabricate, robust to operate in challenging environments, and can exhibit large deformation. However, unlike natural muscles that can actuate at frequencies up to 100 Hz<sup>[3]</sup>, these actuators have low bandwidth (<10 Hz), which makes them unsuitable for building agile robots such as the MIT Cheetah<sup>[4]</sup> and the Harvard RoboBee.<sup>[5]</sup> To achieve animal-like mobility, next generation soft actuators need to have several key properties: 1) high power density for enabling fast locomotion; 2) high bandwidth and good consistency for achieving feedback control; and 3) compatibility with existing power sources and circuitry for realizing power autonomous operation.

In recent years, novel power-dense soft actuators<sup>[6, 7]</sup> have been developed to enable fast locomotion. Aquatic<sup>[8]</sup> and terrestrial<sup>[9]</sup> robots powered by shape memory alloy (SMA) actuators have demonstrated power-autonomous locomotion. However, the actuation frequency of most thermally actuated SMAs is lower than 5 Hz, limiting the robot speed and controllability. To enable impulsive locomotion, Bartlett et al. developed combustion driven soft robots<sup>[10]</sup> and showed their jumping speed can exceed 4 m s<sup>-1</sup>. Yet it remains difficult to implement closed-loop control in these impulsive systems. To achieve high power density and good controllability, thin-film soft actuators<sup>[11, 12]</sup> have been developed to power small scale robots. For example, Wang et al.<sup>[12]</sup> developed microscale electrostatic actuators and incorporated them into an inchworm robot and a surgical device. Liang et al.<sup>[11]</sup> introduced an agile inchworm robot that is powered by 18 μm thick piezoelectric polyvinylidene fluoride (PVDF) actuators. While these examples demonstrate good

controllability, the difficulty of stacking thin films into volumetric actuators and connecting them with complex end effectors has limited thin film actuators to simple designs.

Dielectric elastomer actuators (DEAs) and hydraulically amplified self-healing electrostatic actuators (HASELs) represent another class of soft actuators that are suitable for diverse robotic applications. A DEA is made of an incompressible elastomer layer that is sandwiched by a pair of compliant electrodes. When a potential difference is applied across the two electrodes, electrostatic stress causes the elastomer to deform, and the resulting mechanical strain is used for actuation. A HASEL replaces the elastomeric material with dielectric fluid and uses the hydraulic pressure for its actuation. DEAs and HASELs have demonstrated large strain ( $>100\%$ ),<sup>[13, 14]</sup> high energy density ( $>20 \text{ J kg}^{-1}$ ),<sup>[14, 15]</sup> and integration into robotic manipulators for grasping delicate objects. More recently, highly dynamic silicone DEAs have been developed to drive new aquatic,<sup>[16]</sup> terrestrial,<sup>[6]</sup> and aerial soft robots.<sup>[17]</sup> Among these robots, aerial robots require the highest power density and controllability. Previously,<sup>[17, 18]</sup> we developed a DEA-powered sub-gram flapping-wing micro-aerial vehicle (FWMAV) with the ability to recover from in-flight collisions and perform acrobatic maneuvers such as somersaults. These aggressive flight capabilities have not been demonstrated in the state-of-the-art rigid-powered aerial robots.<sup>[5, 19-23]</sup> However, the performance of FWMAVs with DEAs still lags those with rigid actuators (typically piezoelectric bimorphs) in two key fronts: 1) the actuation voltage of DEAs is approximately 10 times higher than the state-of-the-art piezoelectric bimorphs; and 2) due to the low power density, the lift-to-weight ratio of soft FWMAVs is 45% lower than that of the best rigid FWMAVs. These shortcomings hinder power autonomous flights in soft robots.

Towards overcoming these challenges, two fabrication methods for making power-dense and low voltage DEAs were developed. Duduta et al.<sup>[24, 25]</sup> introduced a method for making power-dense

DEAs through spin coating and stamping. This method makes 30 - 50  $\mu\text{m}$  thick elastomer layers through spin coating, and then transfers compliant electrodes to the elastomer layers through stamping. However, DEAs made of this technique require a high actuation voltage ( $>1$  kV) because the elastomer film quality becomes inconsistent as the spin coating speed increases. In another approach, Ji et al.<sup>[6]</sup> developed highly dynamic (400 - 600 Hz) DEAs capable of operating in the 500 V range. In this method, a pre-stretch step was implemented to reduce the thickness of the actuator film down to 6  $\mu\text{m}$  following which Langmuir method was used to form the electrode using single-wall carbon nanotubes (SWCNTs). While applying pre-stretch is effective in producing high quality thin films and lowering the operation voltage, it introduces two problems. First, applying pre-stretch requires a heavy supporting structure and it reduces the robot's net payload. Second, pre-stretching the SWCNT-electrode lowers electrical conductivity, which reduces efficiency and limits actuator size. For example, the efficiency and size of an existing high bandwidth (500 Hz) DEA<sup>[6]</sup> were limited to 0.95% and 1 mg, respectively. Thus, existing fabrication methods are inadequate in making mesoscale (10 mg – 1 g) DEAs that are efficient ( $>5$  %), low voltage ( $<1$  kV), and high bandwidth ( $>100$  Hz).

In this work, we present a low voltage, long endurance, and power-dense DEA created via a new multiple-layering fabrication method and electrode material optimization. By refining the spin coating and vacuum filtration processes,<sup>[17]</sup> our approach enables high quality 10  $\mu\text{m}$  elastomer thin films and conductive SWCNT electrodes. With this approach, we demonstrate a 20-layer, 143 mg DEA that can operate at 400 Hz and 500 V for over 2 million cycles. The DEA's power density, actuation voltage, and lifetime are comparable to rigid actuators such as piezoelectric bimorphs at a similar size. Based on this DEA, we developed dynamic and aerodynamic models to design a new sub-gram soft aerial robot. The robot demonstrates a high lift-to-weight ratio of 3.7, which is

similar to that of the best rigid-powered FWMAVs. We further built a 4-DEA, 680 mg soft aerial robot for hovering flight demonstrations. The robot flew for 20 seconds with maximum position and attitude errors of 2.5 cm and  $2^\circ$ , respectively. To the best of our knowledge, this is the longest and best performing flight among sub-gram aerial robots. This work shows mesoscale DEAs can operate below 1 kV while exhibiting high power density and long endurance. These features represent an important step towards achieving power autonomous flights in soft aerial robots.

## **2. DEA voltage reduction**

The DEAs fabricated with our approach demonstrate operating voltages reduced to 500 V and lifetimes increased to over 2 million cycles while maintaining high power-density ( $>500 \text{ W kg}^{-1}$ ). A multiple-layer DEA consists of many thin layers of dielectric elastomer that are sandwiched by compliant and interdigitated electrodes. To reduce the driving voltage while maintaining the same output power, we lowered the elastomer layer thickness and increased the total number of layers while maintaining the overall DEA size. This process created two challenges: 1) thin elastomer sheet becomes uneven at higher spin coating speeds due to the surface irregularity caused by inhomogeneous electrodes; and 2) the probability of dielectric breakdown increases as the number of layers (corresponds to net electrode area) increases. To address these challenges, we designed models and experiments to investigate the influence of fabrication processes on DEA quality and performance. We made low voltage DEAs through applying vacuum to improve the elastomer layer quality and optimizing the CNT electrode to reduce the number of defects.

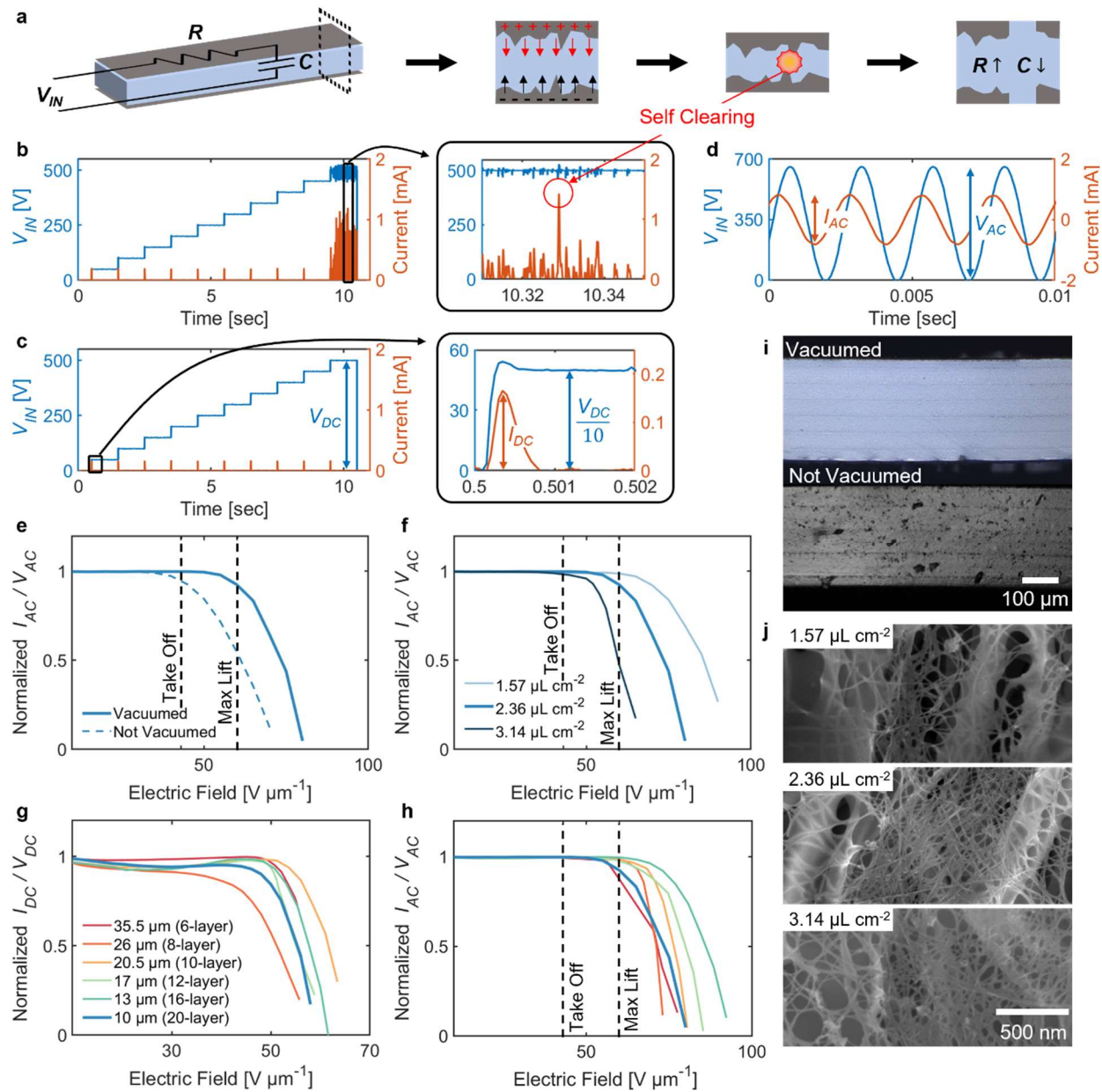


**Figure 1. Characterization experiments of 2-layer DEA samples.** **a)** Illustration of a 2-layer DEA, its electrical model, and the self-clearing process. **b)** Driving voltage and current response during the DC clearing process. The current spikes circled in the inset plot highlights "self-clearing". **c-d)** DC (c) and AC (d) voltage and current measurements after the sample is fully cleared. (c) and (d) show zoomed-in images of the DEA's current response to step (c) and sinusoidal (d) voltage inputs. **e-f)** Comparison of normalized AC conductance as functions of applied electric field between samples of different vacuum conditions (e) and CNT concentrations (f). **g-h)** Normalized DC (g) and AC (h) conductance as functions of applied electric field for DEA samples with different layer thicknesses. The individual layer thicknesses correspond to the ones for making 6, 8, 10, 12, 16, and 20-layer DEAs of the same size. **i)** Confocal microscope images that compare the cross-sections of DEAs with (top) and without (bottom) vacuum process. **j)** Scanning electron microscope (SEM) images of the filters with different CNT concentrations.

First, we used an electrical model to relate DEA's geometry and microscopic properties to its output power. Figure 1a illustrates a 2-layer DEA and superimposes the equivalent electrical model. The DEA consists of a dielectric elastomer layer sandwiched by two compliant CNT electrodes. The DEA resistance  $R$  is contributed by the sheet resistance of the percolative CNT network and the contact resistance between the CNT and the electrical connections. The DEA capacitance  $C$  depends on the elastomer layer's thickness, net area, and dielectric constant. The values of  $R$  and  $C$  determine the output power and efficiency. Given a fixed geometry, the output power increases with decreasing  $R$  and increasing  $C$ .

We used models and experiments to show the values of  $R$  and  $C$  can determine the DEA's quality and performance. In a cross-sectional illustration, Figure 1a shows the microscopic inhomogeneity of the DEA's electrode. Upon actuation, a strong electric field develops around sharp or irregular features, leading to a localized dielectric breakdown. This breakdown generates heat and degrades the nearby CNTs. This type of minor breakdown is called "self-clearing"<sup>[26]</sup> as it removes the local defects without causing permanent failure. Figure 1b shows a "self-clearing" experiment in which we increased the DC driving voltage from 0 V to 500 V in steps of 50 V over 10 seconds. At a high applied voltage of 500 V, we observed small sparks in the DEA. These sparks correspond to the current spikes (highlighted in orange) in Figure 1b. After repeating the same driving signals for several times, all defects were removed and the DEA behaved as an ideal  $RC$  circuit (Figure 1c). To remove all defects in the operating range, we performed DC (Figure 1c) and AC (Figure 1d) clearing tests for every DEA.

Through these clearing tests, we measured  $R$  and  $C$ , and determined DEA peak performance and efficiency. In the DC (Figure 1c) and AC (Figure 1d) tests, the DEA current closely resembled an  $RC$  circuit's step and sinusoidal response, respectively. The values of  $R$  and  $C$  were calculated

based on the current measurements. We found that  $R$  and  $C$  change during the “self-clearing” process. While the “self-clearing” process removes small defects, local dielectric breakdowns create heat and damage the CNT network connections. Consequently, small patches of CNT become disconnected and electrical current cannot flow through these areas. This reduction of net electrode area reduces  $C$  and increases  $R$  (Figure 1a). When the applied voltage is low, there is a small amount of “self-clearing” and the values of  $R$  and  $C$  change slowly. The net output power increases due to an increase of the applied voltage. However, once the applied voltage exceeds a critical value, excessive “self-clearing” occurs, and it burns away large areas of the CNT electrodes. This further causes a sharp increase in  $R$  and a reduction in  $C$ . Consequently, the DEA output power reduces even as input voltage continues to increase. The DC and AC tests on the 2-layer samples identify the DEA operating voltage that maximizes output power.

Figure 1e-h show a suite of 2-layer characterization experiments that illustrate the influence of different fabrication parameters. These plots show DEA conductance as a function of driving voltages. In DC and AC tests, the DEA conductance  $G$  was calculated as:

$$\begin{aligned} \text{DC test: } G &= \frac{1}{R} = \frac{I_{DC}}{V_{DC}} \\ \text{AC test: } G &= \frac{1}{|Z|} = \frac{1}{\sqrt{R^2 + \frac{1}{w^2 C^2}}} = \frac{I_{AC}}{V_{AC}} \end{aligned} \quad (1)$$

In Equation (1),  $Z$  is the complex impedance,  $w$  is the angular frequency,  $I_{DC}$  and  $I_{AC}$  are the current amplitudes, and  $V_{DC}$  and  $V_{AC}$  are the voltage amplitudes. To identify the critical electric field at which the DEA starts to deteriorate due to “self-clearing”, we normalized the driving voltage (divide by the layer thickness) and conductance (divide by the DEA conductance at 0 V) of each test. All plots in Figure 1e-h show a similar trend. The conductance changes slowly at low electric

fields, but sharply decreases at high electric fields. The use of different fabrication parameters shifts the conductance curve horizontally, showing the differences in DEA performance.

Figure 1e and i illustrate the benefit of applying vacuum after spin coating an elastomer layer. At a high spin coating speed ( $>3000$  rpm), the elastomer thin film suffers from two problems: 1) micron-sized air bubbles are trapped in the spin coated layer due to surface irregularities; and 2) macroscale unevenness appears along the edges of the patterned CNT electrodes. We hypothesized that the second problem stems from the friction coefficient difference between the elastomer and the CNT surfaces. During the vacuum process, we observed that the macroscopic nonuniformities are eliminated. In addition, Figure 1i shows two confocal microscope images that compare vacuumed and unvacuumed elastomer cross-sections. The vacuumed elastomer sample is uniform whereas the unvacuumed sample contains many bubbles. These observations suggest that adding a vacuum step substantially increases the DEA's dielectric breakdown field.

Figure 1e compares the conductance relationship of two  $10\ \mu\text{m}$ -thick samples with and without the vacuum process. The conductance of the unvacuumed sample and the vacuumed sample starts to sharply decrease at an applied electric field of  $45\ \text{V}\ \mu\text{m}^{-1}$  and  $60\ \text{V}\ \mu\text{m}^{-1}$ , respectively. Since the DEA power density is proportional to the fourth power of the applied electric field, the result in Figure 1e implies that applying vacuum increases the DEA output power by over 300%. In Figure 1e, we overlaid two vertical lines that indicate the robot takeoff and maximum lift conditions (see Section 5 for details). The unvacuumed sample can barely operate at the takeoff condition whereas the vacuumed sample can operate at the maximum lift condition. This plot indicates that adding the vacuum step is crucial for a DEA with a  $10\ \mu\text{m}$  layer thickness to achieve flight.

In addition to improving the elastomer layer quality, we optimized electrode fabrication by testing different CNT concentrations in the filtration process (See Experimental Section for details about

the filtration process). The CNT concentration influences DEA resistance and breakdown field. The use of a higher CNT concentration forms a denser percolative network and this reduces resistance. According to our  $RC$  circuit model, a lower resistance leads to a higher voltage drop across the equivalent capacitor, and this increases the DEA output power. However, a denser percolative network contains more defects such as microscopic CNT clusters, which reduce the breakdown field. An optimal CNT concentration should balance these two tradeoffs.

Figure 1f and j compare three samples with different CNT concentrations. In Figure 1j, the SEM images show the CNT network becomes denser as the CNT concentration increases. For this range of CNT concentration, the electrode thickness is estimated to be less than 30 nm, which is over 300 times smaller than the elastomer layer thickness (10-36  $\mu\text{m}$ ). We did not observe change of elastomer thickness, adhesion property, or uniformity when varying the CNT concentration from 1.57 to 3.14  $\mu\text{L cm}^{-2}$ . Figure 1f compares the samples' breakdown fields at the 400 Hz AC testing conditions. This driving frequency is chosen based on the robot hovering condition. The DEA characterization experiments (Section 4) and robot flight demonstrations (Section 5) are conducted at the same frequency. It shows the sample breakdown field increases as the CNT concentration decreases. While the 3.14  $\mu\text{L cm}^{-2}$  sample has the smallest resistance, it experiences a large amount of "self-clearing" at the maximum lift condition. A DEA with this CNT concentration has limited maximum output power due to excessive "self-clearing". In contrast, the sample with the smallest CNT concentration shows the highest breakdown field. However, compared with the 2.36  $\mu\text{L cm}^{-2}$  sample, the 1.57  $\mu\text{L cm}^{-2}$  sample's sheet resistance increases by over 360%. According to our model, the voltage drop across the equivalent capacitor reduces by over 20% when the sample operates at 400 Hz. This implies the maximum output power of the 1.57  $\mu\text{L cm}^{-2}$  sample is smaller than that of the 2.36  $\mu\text{L cm}^{-2}$  sample. These experiments show the optimal CNT concentration

should be determined based on the DEA's operating conditions. Given a desired operating frequency and DEA capacitance, one should choose the lowest CNT concentration that ensures 90% of the total voltage is applied across the capacitor (See Supporting Information S1 for detailed equations and analysis).

After optimizing the CNT concentration and introducing a new vacuum step, we fabricated and tested 2-layer samples (consist of 2 electrode layers) of different thicknesses while using the same CNT concentration ( $2.36 \mu\text{L cm}^{-2}$ ) and vacuum process. To reduce the operating voltage from 1800 V to 500 V, we decreased the elastomer layer thickness from 36  $\mu\text{m}$  to 10  $\mu\text{m}$ . Figure 1g and h show the DC and AC tests of six different samples. These thicknesses were chosen for fabricating multiple-layer (6 to 20 layers) DEAs that will be presented in Section 4. The cumulative thicknesses (layer number multiplied by individual layer thickness) of these DEAs are similar. All tests presented in Figure 1 used 2-layer samples, and later sections will present data involving multiple-layer DEAs with these layer thicknesses. In these DC and AC tests, all 2-layer DEA samples show similar breakdown fields. This is a significant result that shows our fabrication method produces high quality thin elastomer films in the 10 – 36  $\mu\text{m}$  range, and it implies DEAs of a smaller elastomer thickness can demonstrate similar mechanical performance under a lower actuation voltage.

### **3. Multiple-layer fabrication and robot construction**

The previous section described results on making low-voltage 2-layer DEA samples. This section introduces a multiple layer fabrication process for low-voltage DEAs and soft aerial robots. Figure 2a illustrates the high-level fabrication procedures in which we first construct the elastomer-electrode multi-layers, then cut and extract a piece, roll it into a cylindrical shell, attach electrical connections, and finally install it into a robot airframe. Figure 2b shows the details of the multiple-

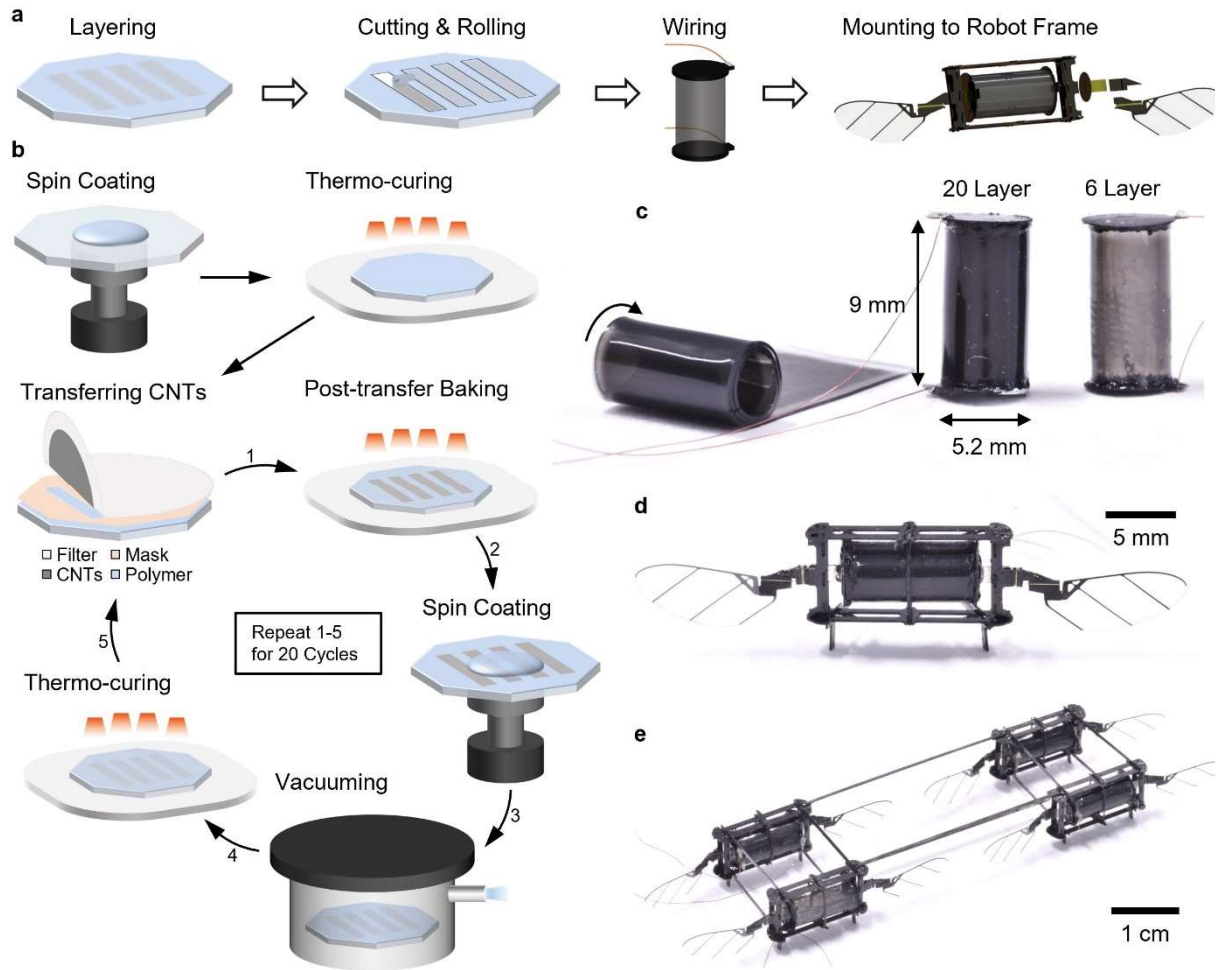


**Figure 2. DEA fabrication and robot assembly.** **a)** Illustrations of DEA and robot fabrication processes. The robot consists of an airframe, a DEA, a pair of wing hinges, wings, and transmissions. **b)** DEA multiple-layering fabrication steps that include post transfer baking, spin coating, vacuuming, thermo-curing, and CNT transferring. **c)** An image illustrating the DEA rolling process and two DEAs made of 6 and 20 electrode layers. **d)** A prototype of the single unit flapping robot equipped with a 20-layer DEA. **e)** An isometric view of a flapping wing microrobot with four units.

layering process improved from our prior work.<sup>[17]</sup> Previously we found that the elastomer curing time grew exponentially as the number of layers increased. Based on our old procedure, it would have taken approximately two days for the 20<sup>th</sup> layer to cure, and this severely limits fabrication scalability. We hypothesize that this is caused by chemical contamination in the elastomer curing process. The surfactant from the bottom elastomer layers and the CNT electrodes slows down the

elastomer curing process. To remove this effect, we added a post-transfer baking step immediately after the CNT transfer (Figure 2b arrow 1). We found this post-transfer baking step is effective in maintaining a consistent elastomer curing time. Supporting Table S1 documents all the steps for fabricating 20 layers of elastomer and electrodes. Next, the planar elastomer DEA was cut and rolled into a cylindrical shell (Figure 2c). Carbon fiber caps with copper wires were attached on both sides of the DEA (See Supporting Information S2.1 for details on making electrical connections). Figure 2c shows an image of the 20-layer DEA and the 6-layer DEA. The 6-layer DEA has a higher transparency as it contains a smaller number of CNT layers. Based on this multiple-layering process, we fabricated six DEAs with different layer thicknesses and number of layers. Table 1 shows the spin coating speed, layer thickness, weight, equivalent capacitance, and resistance of these DEAs. Their performance such as blocked force, displacement, and efficiency will be reported in Section 4.

Finally, we installed a DEA into a robot airframe (Figure 2d) to construct a 167 mg FWMAV. To achieve controlled flights, we assembled 4 robot modules into a 680 mg robot (Figure 2e) to generate control forces and torques. (See Supporting Information S2.2 for details on four-module robot assembly). Section 4 will discuss the design of key robot parameters and Section 5 will describe flight results.

**Table 1.** Features of the DEAs with 6, 8, 10, 12, 16, and 20 layers

Number of layers	Spin coating speed [rpm] (First/Intermediate/Top)	Thickness of central layers [ $\mu\text{m}$ ]	Total thickness [ $\mu\text{m}$ ]	Weight [mg]	Capacitance [nF]	Resistance [ $\text{k}\Omega$ ]
6	2100/1500/2400	35.5	223	125	1.83	22.1
8	3000/2000/3000	26	225	123	3.35	17.8
10	3000/2600/3500	20.5	220	132	4.89	14.4
12	3600/3100/4300	17	218	128	7.22	8.82
16	5000/4100/6000	14	234	144	13.2	7.89
20	6000/5500/7000	10	213	143	20.0	4.45

#### 4. Actuator characterization and robot design

We tested six DEAs of different layer thicknesses (10 – 36  $\mu\text{m}$ ) and showed they exhibit similar blocked force, displacement, bandwidth, and output power. These DEAs consist of different number of layers (6 – 20 layers) such that the total thickness and the actuator weight remain similar (Table 1). Based on the DEA characterization experiments, we developed a new quasi-steady aerodynamic model for designing the robot. The new model informs key design parameters such as the transmission ratio and the wing hinge stiffness. We constructed new robots and conducted static flapping experiments. Furthermore, we showed the 20-layer DEA can achieve takeoff flight at a low driving voltage of 475 V. Owing to the new fabrication steps from Section 2 and 3, the DEA endurance substantially increased to well above 2 million cycles.

First, we measured the DEAs' power density and efficiency when they drive flapping-wing robots at flight conditions. A DEA's output power  $p_{out}$  is calculated as:

$$p_{out} = \frac{1}{2} F_B \delta f \quad (2)$$

where  $F_B$ ,  $\delta$ , and  $f$  are the DEA's blocked force, in-robot displacement, and operating frequency, respectively. Equation (2) assumes that a DEA's force and displacement relationship is linear at small ( $<0.15$ ) strain values.<sup>[24,26]</sup> Figure 3a illustrates the blocked force experiments in which we placed the DEA under a Nano17 Titanium force sensor and applied a 400 Hz sinusoidal voltage signal (See Supporting Information S3 for details). Based on previous studies,<sup>[17,25]</sup> a DEA's blocked force is approximately constant at frequencies below its electrical resonance. Hence, the DEA blocked force was measured only at the robot hovering frequency. Figure 3b shows the blocked force measurements of the six DEAs as functions of electric field. The electric field is calculated as the applied voltage divided by the corresponding DEA layer thickness (3<sup>rd</sup> column

of Table 1). These DEAs with different layer thicknesses generate similar blocked forces (0.36 – 0.38 N) in a similar range of electric field (50 – 60 V  $\mu\text{m}^{-1}$ ). This result shows that a DEA with thinner layers can generate similar forces at a lower driving voltage.

Next, we measured the DEA displacement when it drove the robot at the 400 – 500 Hz frequency range. We installed each DEA into a robot airframe (Figure 3c) and filmed flapping-wing experiments at different driving voltages and frequencies. DEA displacement is defined as the distance between its maximum elongation and minimum retraction (Figure 3c). The DEA displacement varies as the driving frequency changes, and its frequency response depends on the robot design parameters such as wing area, inertia, transmission ratio, and wing hinge stiffness. Supporting Information S3 and Figure S5 show the displacement measurements for the six DEAs at different driving frequencies and voltages. Figure 3d compares displacement as functions of driving electric field for the six DEAs when they were driven at 400 Hz, and they all exhibit a similar trend.

For the 6-layer and 20-layer DEAs, we gradually increased the driving voltage until the DEA displacement reaches 1.15 mm. This operating condition corresponds to the maximum robot lift. Section 5 will report lift measurements of the robots powered by the 6-layer and 20-layer DEAs. For the 8, 10, 12, and 16-layer DEAs, we stopped increasing the driving voltage once their displacements exceed 0.8 mm, which corresponds to the robot hovering condition. The 8, 10, 12, and 16-layer DEAs were not used in flight tests, hence we did not drive them up to maximum operating conditions in static flapping experiments. These experiments show the 20-layer DEA can achieve a high displacement (1.15 mm) at a low driving voltage (630 V). When driven with 400 Hz and a similar electric field, the 6-layer and 20-layer DEAs exhibit similar blocked force and in-robot displacement. Based on Equation (2), we calculated the maximum output power of

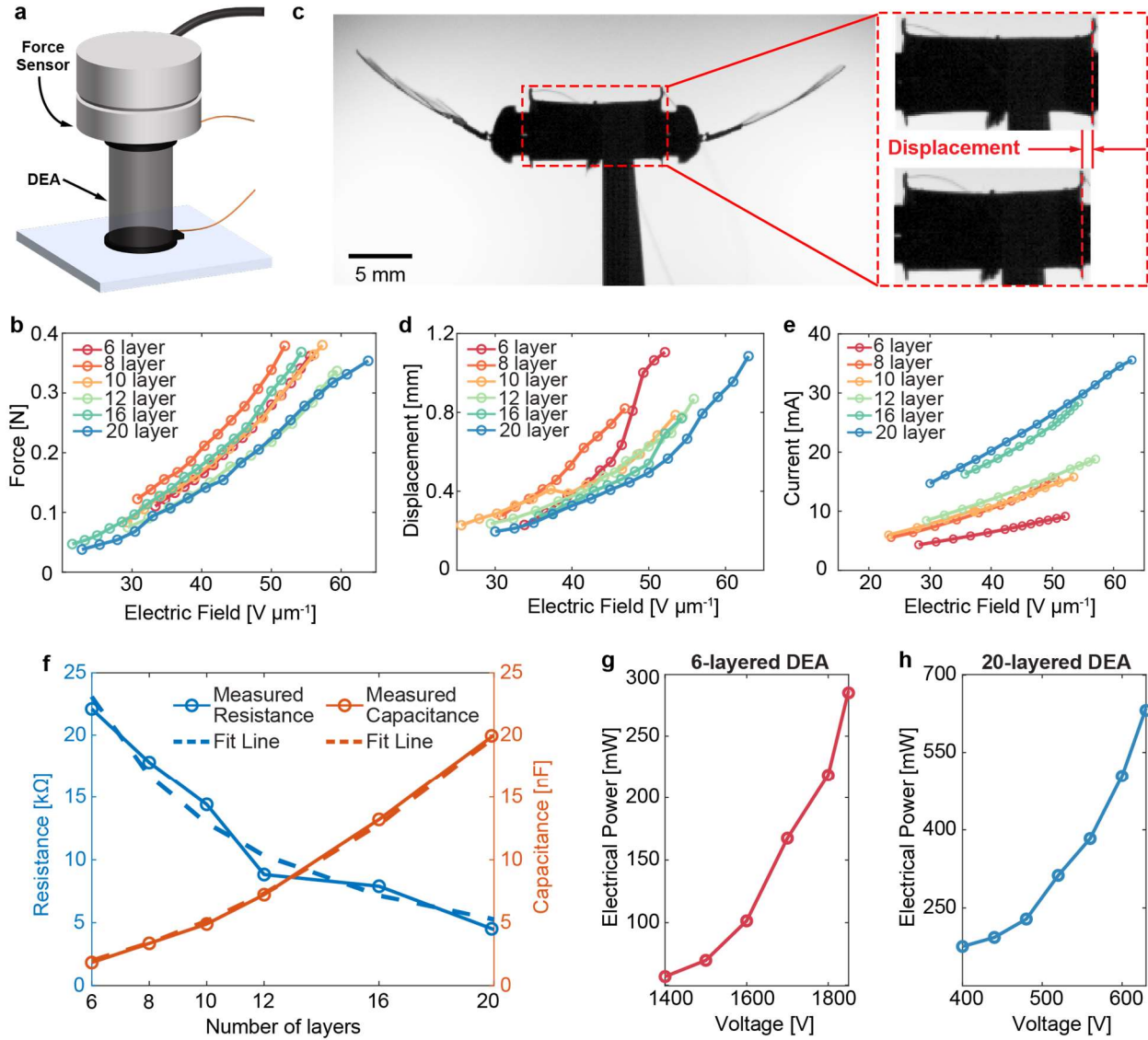


**Figure 3. Characterization of DEA performance.** **a)** Experimental setup for measuring the DEA blocked force. **b)** Blocked force as a function of applied electric field. **c)** Experimental setup for measuring the DEA in-robot displacement. **d-e)** DEA displacement (**d**) and current magnitude (**e**) as functions of applied electric field. **f)** Measured DEA resistance and capacitance as a function of layer number. **g-h)** Power consumption of the 6-layer (**g**) and 20-layer (**h**) DEAs as a function of driving voltage. The driving frequency in all experiments is set to 400 Hz.

the 6-layer and 20-layer DEAs to be 65.7 mW and 76.9 mW, respectively. Compared with the 6-layer DEA, the 20-layer DEA exhibits similar output power at one-third the driving voltage.

Next, we measured the DEAs' capacitance, resistance, power consumption, and efficiency. The driving frequency was set to 400 Hz in these experiments. Figure 3e shows the DEAs' peak-to-

peak current amplitude as a function of the applied electric field. The DEA current increases as the number of layers increases. According to the electrical model, an increase in the number of DEA layers corresponds to an increase in the capacitance  $C$  and a decrease in the resistance  $R$ :

$$C = n \frac{\varepsilon_0 \varepsilon_r A}{t_{layer}} = n^2 \frac{\varepsilon_0 \varepsilon_r A}{t_{tot}} = C_0 n^2 \quad (3)$$

$$R = R_0 \frac{1}{n} \quad (4)$$

In Equation (3),  $n$  is the DEA layer number,  $\varepsilon_0$  is the permittivity of free space,  $\varepsilon_r$  is the elastomer dielectric constant,  $A$  is the area of a single layer,  $t_{layer}$  is the thickness of a single layer, and  $t_{tot}$  is the total DEA thickness. Since a DEA deforms during actuation,  $R$  and  $C$  change at different driving voltages. To calculate  $R$  and  $C$  at the robot hovering condition, Equation (3) and (4) need to use the mean area  $A$  and thickness  $t_{layer}$  during actuation. At the robot hovering condition,  $A$  and  $t_{layer}$  are approximately 10% larger and 5% smaller than that at the uncharged conditions. In Equation (3) and (4),  $R_0$  and  $C_0$  are lumped resistance and capacitance parameters. The solid lines in Figure 3f show the measured  $R$  and  $C$  as a function of the DEA layer number. (See Supporting Information S4 for details on capacitance and resistance measurements). The dotted lines show the best fit curves based on Equation (3) and (4) where  $R_0$  and  $C_0$  are 153 k $\Omega$  and 0.050 nF, respectively. This comparison shows that Equation (3) and (4) accurately describe the scaling relationships of  $R$  and  $C$  as the layer number increases.

Furthermore, we measured the power consumption of the 6-layer and 20-layer DEAs at flight conditions (Figure 3g-h). At maximum operating conditions, the 6-layer and 20-layer DEAs consume 287 mW and 636 mW, respectively. Based on the output power, the 6-layer and 20-layer DEA transduction efficiency are 22.9% and 12.1%, respectively. Although DEAs with a larger

number of layers operate at lower voltages, they consume higher power and have lower efficiency. This reduction of transduction efficiency is predicted by the *RC* circuit model and the scaling analysis (See Supporting Information S4 for details).

After characterizing the DEA performance, we redesigned the robot to maximize net lift. Prior works designed key robot parameters using a scaling analysis.<sup>[17, 18]</sup> While this approach enabled robot flight, the robot aerodynamic efficiency was substantially lower compared with other FWMAVs. In this work, we derived a 2 degrees-of-freedom (DoFs) quasi-steady aerodynamic model and used the model to aid robot design (See Supporting Information S5 for details). The model takes the DEA's output power as the input, and it calculates the resulting flapping kinematics and aerodynamic forces. By varying kinematic and design parameters such as flapping frequency, transmission ratio, transmission stiffness, and wing inertia, we simulated different designs and evaluated their performance. After identifying a desired robot design in simulation, we built new robots and conducted static flapping experiments.

Figure 4a-g compare model predictions (a,b,d,f) and experimental measurements (c,e,g). Based on the DEA's blocked force measurement, we simulated a flapping experiment where the DEA was operated with 630 V and 400 Hz. Figure 4a and b show the top (a) and side (b) views of the flapping-wing motion in one period. The flapping-wing motion is reciprocal, and it consists of wing stroke motion and pitch rotation.<sup>[27]</sup> Figure 4a illustrates the simulated downstroke and upstroke motion, and Figure 4b illustrates the passive wing pitch rotation. Figure 4d shows the stroke and pitch kinematics at this operating condition. The simulation predicts the time averaged lift force to be 2.77 mN per wing. Furthermore, we varied the driving voltage and frequency in the range of 300 – 630 V and 400 – 450 Hz, and calculated the corresponding wing stroke motion, pitch motion, and net lift. Figure 4f shows the simulated peak-to-peak stroke amplitude as

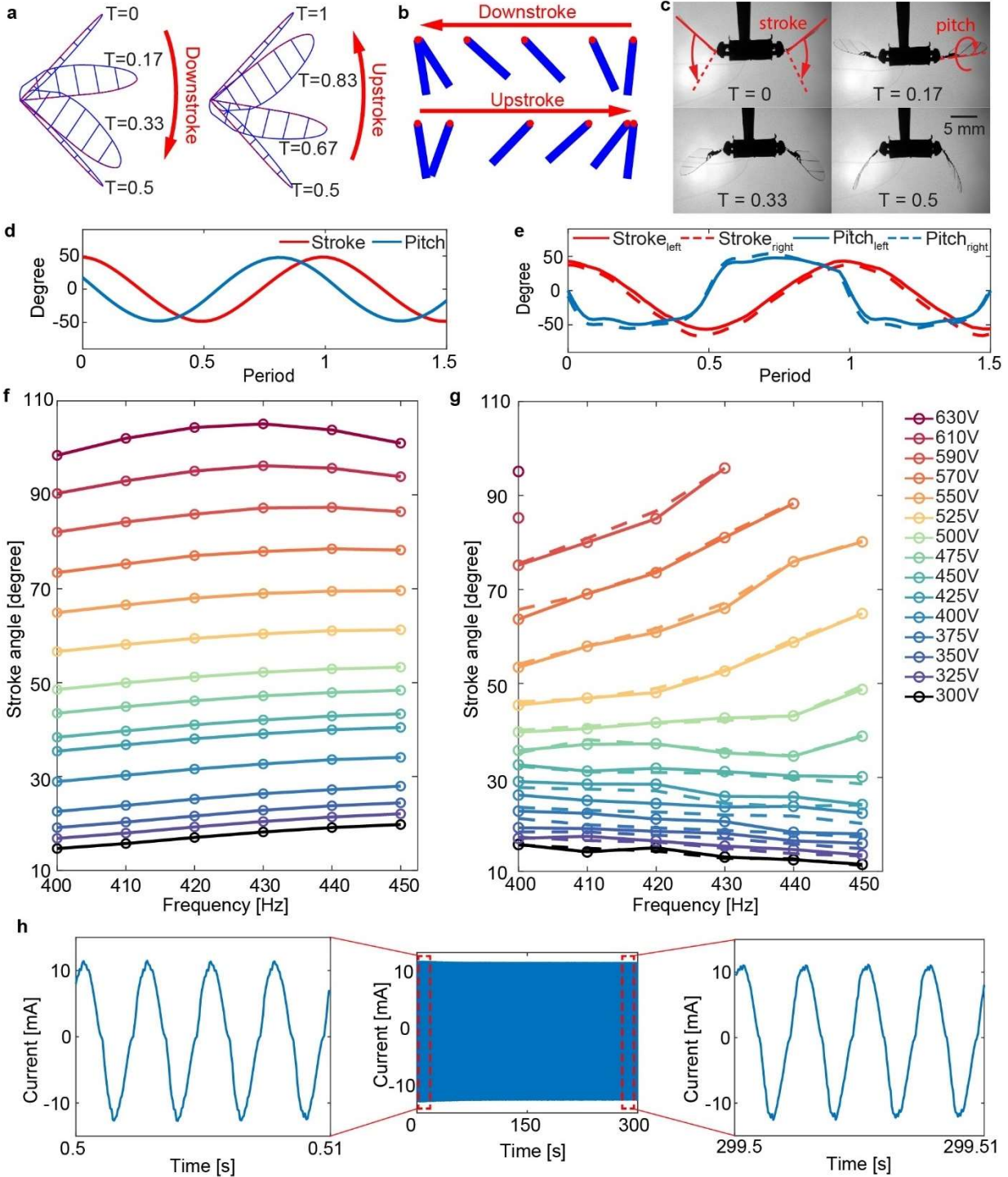


**Figure 4. Robot flapping-wing simulations and experiments. a-b)** Top view (a) and side view (b) images of simulated flapping-wing kinematics. **c)** An image sequence showing the flapping motion of a robot driven by the 20-layer DEA. **d-e)** Simulated and tracked wing stroke and pitch motion of the robot's left and right wings. In (a), (c), (d), and (e), time  $T$  is normalized to one flapping period. **f-g)** Simulated and tracked wing stroke amplitude as functions of driving voltage and frequency. **h)** Current response of a 300-second endurance test conducted on the 20-layer DEA.

functions of driving voltage and frequency. The corresponding wing pitch amplitude and net lift are shown in Figure S7c-d. These simulations predict that the new robot design would achieve over 60% higher net lift.

Figure 4c, e, and g show the experiments agree well with the simulations. Figure 4c shows an image sequence that illustrates half of a flapping period. Figure 4e shows the robot stroke and pitch kinematics when it was driven with 630 V and 400 Hz. The tracked wing stroke motion (red) closely resembles the simulated result in Figure 4d, but the tracked pitch motion (blue) has higher harmonics that are absent in the simulation. This modeling error is mainly contributed by two factors: (1) lack of modeling terms that account for rotational forces and aerodynamic damping during the wing pitch rotation,<sup>[27,28]</sup> and (2) simplified approximation that the wing hinge is a linear torsional spring.<sup>[29]</sup> Consequently, ignoring these nonlinear effects causes a 10-15% error in the lift predictions (See Supporting Information S5 for details of the dynamic model). Next, we operated the robot at the same range of operating conditions as in the simulations. Figure 4g shows the experimental measurements have a similar trend compared with the simulations in Figure 4f. In experiments, the robot wing experienced large deformation at a combination of high operating voltage and frequency. This would be detrimental to the robot's lifetime; hence we only operated the robot at 400 Hz for the 610 V and 630 V cases. In summary, the new quasi-steady model informed robot designs and predicted an over 60% lift improvement. The experimentally measured flapping kinematics showed good agreement with the simulations (See Supporting Video 1 for comparison). Section 5 will report on the robot lift measurement. Furthermore, we demonstrated DEA's endurance substantially improves in long duration flapping tests. Our prior work<sup>[17]</sup> reported a DEA's lifetime of 600,000 cycles while the wing hinge lifetime is approximately 1.5 million cycles. Consequently, the lifetime of the previous soft aerial robot was limited by the

DEA's endurance. We hypothesized that the new DEA's lifetime will increase because the vacuum step removes the air bubbles and the macroscopic nonuniformities in the elastomer layers. The new fabrication procedures reduce the number of defects in elastomer and electrodes. Figure 4h shows a 300 second endurance experiment in which the 20-layer DEA was driven at 500 V and 400 Hz. Over this 300 second duration, the change of instantaneous DEA current was less than 0.5%. Cumulatively, both the 6-layer and the 20-layer DEAs were driven for over 2 million cycles at the robot hovering conditions (See Supporting Information S6 for details), and no damage or performance degradation was observed during the tests. These experiments imply the new DEAs' lifetime may be well above 2 million cycles, demonstrating a significant performance improvement in power-dense soft actuators.

## **5. Robot lift measurements and flight demonstrations**

In addition to improving the robot's lifetime, we demonstrated an over 70% increase in the robot lift and substantially enhanced the hovering flight performance. First, we mounted the robot on a balance beam that can rotate with respect to a pivot point (Figure 5a). For a given driving voltage and frequency, the robot flies upward if the net lift force exceeds its weight. The liftoff voltage is defined as the driving voltage at which the net lift force equals the robot weight. For a driving voltage higher than the liftoff voltage, we placed a dummy weight on the balance beam to measure the higher lift force.

Figure 5b shows a liftoff experiment of a robot powered by the 20-layer DEA. This robot weighs 167 mg and a 400 mg payload was attached to the balance beam. The frequency and amplitude of the driving signal were set to 400 Hz and 630 V, respectively. The liftoff experiment was filmed with a Phantom v7.1 high speed camera at 22000 frames per second (fps), and the robot position was tracked through analyzing the takeoff video. Figure 5b shows the robot lifts up by

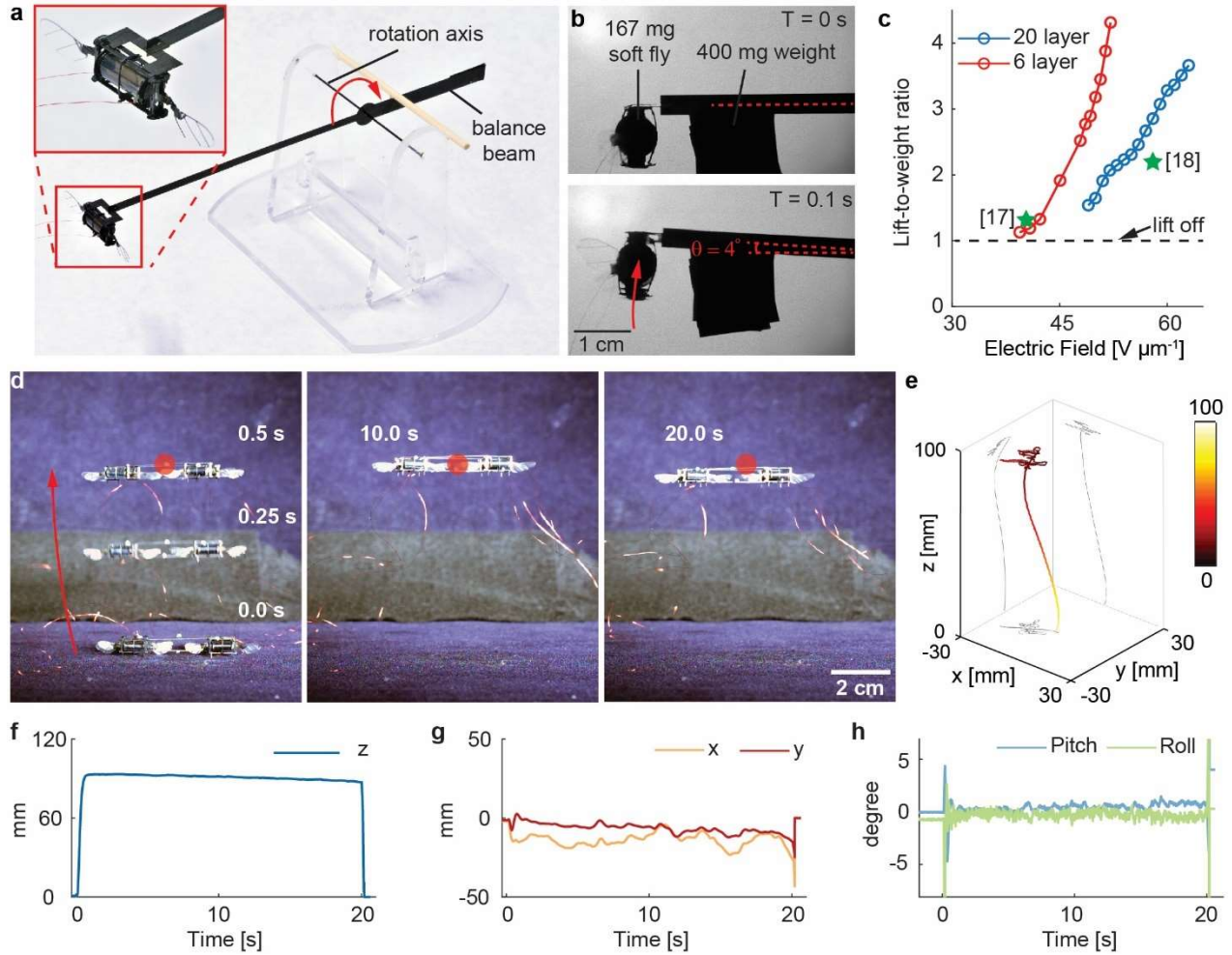


**Figure 5. Robot liftoff and hovering flight experiments.** **a)** We mount the robot on a balance beam to measure its net lift force. **b)** Two images that show the robot lifts off a 400 mg payload when driven at 630 V and 400 Hz. The net robot lift is 601 mg and the maximum lift-to-weight ratio is 3.7. **c)** Measured lift-to-weight ratios of the robots powered by the 20-layer and 6-layer DEAs, respectively. The green stars represent the maximum lift-to-weight ratios of our previous works. **d)** An image sequence that shows a 20-second hovering flight. **e)** The tracked flight trajectory corresponding to the flight in (d). The color scale represents the distance to the setpoint. **f-h)** The tracked robot altitude (f), x and y positions (g), and attitude (h). During this hovering flight, the maximum position and attitude errors are 2.5 cm and 2°, respectively.

approximately 1 cm in 0.1 s. Supporting Video 2 shows the same liftoff experiment. Using a tracking algorithm and a dynamical model from a previous study,<sup>[18]</sup> we calculated the net lift force to be 5.89 mN (equivalent to 601 mg), resulting in a lift-to-weight ratio of 3.7.

For the 20-layer DEA, we repeated the liftoff experiment by varying the driving voltage from 500 V to 630 V in steps of 10 V. We also conducted liftoff experiments for the 6-layer DEA powered robot and varied the driving voltages from 1400 V to 1850 V. Figure 5c shows the lift-to-weight ratio of both robots at different driving voltages. To account for different DEA layer thicknesses, we normalized the x-axis to the applied electric field ( $\text{V } \mu\text{m}^{-1}$ ). These liftoff experiments show the maximum robot lift-to-weight ratio of the 6-layer and 20-layer DEAs are 4.3 and 3.7, respectively. These results represent an over 70% lift increase compared with the best existing soft aerial robot.<sup>[18]</sup>

Furthermore, we constructed a 680 mg soft aerial robot that consists of four modules. One robot module is powered by a 20-layer DEA and the other three are powered by 6-layer DEAs. We used one 20-layer DEA due to having only one high voltage and high current amplifier (Trek PZD350) that can supply sufficient current ( $\sim 40$  mA). The other 6-layer DEAs were driven by lower current amplifiers (Trek 2220). Using an existing motion tracking arena<sup>[5]</sup> and a geometric flight controller,<sup>[17]</sup> we demonstrated a 20-second hovering flight (Supporting Video 3). Figure 5d shows a composite image sequence of this 20-second flight. Figure 5e shows the flight trajectory, and the color scale represents the distance between the robot and the desired hovering setpoint. Figure 5f-h show the tracked robot altitude (f), x and y positions (g), and the pitch and roll angles (h). During this 20-second hovering flight (excluding takeoff and landing), the maximum position error and attitude error are 2.5 cm and  $2^\circ$ , respectively. Compared with our previous work,<sup>[18]</sup> the flight time increases by 100% and the maximum error reduces by over 50%. To the best of our knowledge, this flight is the longest and best performing (with minimal attitude and position errors) among sub-gram aerial robots.

## 6. Discussion and conclusion

In summary, we developed novel design and fabrication methods for making a low voltage ( $\sim 500$  V), power-dense ( $>500$  W kg<sup>-1</sup>), and long endurance ( $>2$  million cycles) DEA. We also derived a quasi-steady dynamic model for the redesign of a DEA-powered aerial robot. The robot powered by the 20-layer DEA lifts off at 475 V and 400 Hz, and it achieves a high lift-to-weight ratio of 3.7 when the driving voltage increases to 630 V. The 20-layer DEA was driven for over 2 million cycles at the robot hovering condition of 500 V and 400 Hz. Furthermore, we demonstrated liftoff flights and a 20-second controlled hovering flight. The hovering flight represents the longest and best-performing (minimal attitude and position errors) flight conducted by sub-gram aerial robots. Compared with existing soft aerial robots<sup>[17,18]</sup>, there are three transformative performance improvements: 1) a substantial driving voltage reduction of power-dense DEAs for robotic flights (from 1800 V to 500 V); 2) an over 70% increase of the robot lift-to-weight ratio (from 2.2 to 3.7); and 3) a significant increase of DEA lifetime (from 600,000 cycles to well above 2 million cycles).

These results were enabled by novel design and fabrication methods. From a design perspective, we optimized the CNT solution concentration through investigating the tradeoff between having a low bulk resistance (high CNT concentration) and a high dielectric breakdown voltage (low CNT concentration). Given a fixed DEA size and a desired bandwidth, we chose the optimal CNT concentration that balances the tradeoffs. Specifically, the CNT concentration was set as low as possible while the DEA's time constant ( $\tau = RC$ ) remains smaller than the desired actuation period. From a fabrication perspective, we introduced two additional steps to improve the multiple-layering process. First, we added a post-transfer baking step after the CNT transfer. This ensures each elastomer layer has the same curing time (5 minutes). Second, we added a vacuum step to remove the air bubbles trapped in the elastomer layer. This step increases the DEA breakdown

field by 20%. These new design and fabrication methods lead to power-dense and low voltage DEAs, which represent a major contribution to the field of soft actuation.

Furthermore, this work substantially improved DEA performance to the extent that our soft robot becomes comparable to the rigid-powered sub-gram aerial robots in several key metrics. Table 2 gives a detailed comparison of existing sub-gram aerial robots. Rigid sub-gram aerial robots are driven by piezoelectric,<sup>[5, 19, 30]</sup> electrohydrodynamic,<sup>[22]</sup> and electromagnetic<sup>[23]</sup> actuators. The piezoelectric-driven FWMAVs are the best-performing robots that have demonstrated versatile functions such as hovering,<sup>[5]</sup> perching,<sup>[30]</sup> yaw control,<sup>[31]</sup> laser-powered,<sup>[21]</sup> and solar-powered<sup>[19]</sup> flights. The best-performing robot<sup>[19]</sup> has demonstrated an impressive lift-to-weight ratio of 4.1 and a high transduction efficiency of 81%.

**Table 2.** Performance comparison of sub-gram aerial robots

	Weight [mg]	Max lift [mg]	Max lift to weight ratio	Maximum operating voltage [V]	Flapping frequency [Hz]	Power consumption [mW]	Actuator efficiency	Lift to power ratio [mN W <sup>-1</sup> ]	Controlled hovering flight	Ref.
Robots powered by rigid actuators										
RoboBee X-Wing	90	372	4.1	210	165	35	81%	106	Yes	[19]
BigBee	265	450	1.73	200	70	-	-	-	Yes	[32]
Robofly	86	>216	>2.5	190	170	-	-	-	Yes	[21]
Robofly (four wings)	143	305	2.1	190	170	-	-	-	Yes	[33]
Bee <sup>+</sup>	95	143	1.5	260	100	-	-	-	Yes	[20]
EHD robot	30	>67	>2.2	2000	-	693	-	0.948	-	[22]
EM robot	80	>80	>1	1.2	80	1200	-	0.653	-	[23]
Robots powered by soft actuators										
SoftFly V1	155	186	1.2	1350	280	450	5.6%	4.05	Yes	[17]
SoftFly V2	155	341	2.2	2000	500	320	37.5%	10.44	Yes	[18]
SoftFly V3-6 Layer	150	645	4.3	1850	400	287	22.9%	22.5	Yes	This work
SoftFly V3-20 Layer	162	601	3.7	630	400	636	12.1%	9.26	Yes	This work

Compared with the best piezoelectric-driven robot,<sup>[19]</sup> previous soft aerial robots have substantially worse lift-to-weight ratio, endurance, efficiency, and flight performance. In addition, their operating voltage is 10 times higher. In contrast, the new soft robot presented in this work (last two rows of Table 2) achieves a similar lift-to-weight ratio to that of the best rigid sub-gram FWMAV. While the driving voltage is 2-3 times higher than that of the piezoelectric robots, there exists sub-gram power electronics capable of supplying 500 V.<sup>[6]</sup> Furthermore, our soft aerial robot shows several advantages over the rigid sub-gram FWMAV. First, the DEAs can easily scale up while the piezoelectric actuator's power density reduces at a larger size.<sup>[32]</sup> Row 2 in Table 2 shows the performance metric of a scaled-up FWMAV named "BigBee".<sup>[32]</sup> Although the robot weight increases by approximately 3 times, the robot lift-to-weight ratio reduces to 1.7. Our soft robot has a larger weight and the highest payload, hence it can carry more sensors and electronic components. Second, our soft robots are more robust than rigid robots. They can demonstrate acrobatic maneuvers such as somersault and in-flight collision recovery. These insect-like flight capabilities are important for future FWMAVs to navigate in cluttered environments and fly in swarms. Third, our soft robot shows longer flight endurance and better hovering performance. While most existing sub-gram FWMAVs<sup>[19, 20, 31]</sup> demonstrate short-duration flights that are less than 5 seconds, this work presents the longest flight with the smallest position and attitude errors. These results demonstrate the potential of highly agile and robust robots powered by soft artificial muscles.

Despite achieving substantial progress in this work, our soft robot remains less efficient than piezoelectric FWMAVs. In Table 2, columns 7-9 compare power usage, actuator efficiency, and lift-to-power ratio. Compared with the best-performing FWMAV, our 6-layer DEA consumes 8.2 times more power but only provides 70% more lift. Our 20-layer DEA consumes 18 times more power but provides 60% more lift. Based on the lift-to-power comparison, the 6-layer and 20-layer

DEAs are 4.7 and 11.4 times worse than the piezoelectric actuators. This shortcoming not only means the DEAs are less efficient, but also poses challenges for developing power electronics. While our fabrication method can produce thinner elastomer layers ( $\sim 5 \mu\text{m}$ ), our amplifier cannot drive lower voltage DEAs because its maximum current supply is limited to 40 mA. Supplying such a high current is a substantial challenge for sub-gram power electronics. Towards achieving power autonomy in soft aerial robots, future work should focus on improving transduction efficiency through lowering the electrode resistance. In preliminary experiments, we found that the DEA resistance is primarily contributed by the contact resistance between the CNT electrodes and the carbon fiber connectors. Future studies should explore new electrode materials and fabrication techniques for reducing DEA contact resistance. To further improve the lift-to-power ratio, future studies should reduce the robot flapping frequency and increase the wing area.<sup>[34]</sup> We believe that reducing DEA electrode resistance and improving robot aerodynamic efficiency represent the next major steps toward enabling power autonomous flights in soft robots.

## 7. Experimental Section

This section presents the multiple-layering DEA fabrication process that corresponds to Figure 2b. First, 150  $\mu\text{L}$  CNT solution (Invisicon 3500) was dispersed in 20 mL isopropyl alcohol (IPA). The solution was sonicated for 2 minutes, and then it was poured over a 90 mm diameter polytetrafluoroethylene (PTFE) filter (Satorius 7022P). Next, the solvent with IPA was filtrated through vacuum which evenly spread the remaining CNTs on the top surface of the filter. The calculated areal density was 2.36  $\mu\text{L cm}^{-2}$ . The filters with the transferred CNTs were placed at room temperature for 48 hours to be fully dried.

The uncured elastomer (Elastosil P7670, Wacker) was prepared by mixing equal amount of part A and B in a mixer (AR-100, Thinky), and it was spin-coated (G3P-8, SCS) on top of an acrylic substrate. The spin speeds for each layer are reported in Table S1, and faster speeds were used for the first and the top layers to make thinner layers. This contributes to a stronger electrostatic attraction between the top and bottom electrodes after rolling the DEA into a cylindrical shell. Next, the spin-coated elastomer was placed in a vacuum (3 kPa) for 3 minutes, and then the substrate was baked in a 60 °C oven. The baking time was adjusted for different layers (see Table S1) with the goal of maintaining a consistent level of stickiness on the surface of the cured elastomer.

The CNTs were then transferred from the filter to the top surface of the elastomer through a mask with electrode patterns. Two types of masks were prepared and used alternately for each layer so that the CNTs in the odd and even layers could be connected to opposite electrical terminals. Next, the substrate with the transferred CNT electrodes underwent a post-transfer baking process at 60 °C for 3 minutes. The steps from spin-coating to post-transfer baking constituted one cycle of the multiple-layering process. This cycle was repeated 20 times to make the 20-layer DEA.

## **Acknowledgements**

We thank Gloria Zhu for discussion and proofreading. This work was supported by the Research Laboratory of Electronics, MIT under the Research Support Committee Grant 2244181.

## References

- [1] C.-P. Chou, B. Hannaford, *IEEE Trans. Robot.* **1996**, *12*, 90.
- [2] J. P. Whitney, M. F. Glisson, E. L. Brockmeyer, J. K. Hodgins, presented at *IEEE Int. Conf. Intell. Robots Syst.* Chicago, IL, September **2014**.
- [3] F.-O. Lehmann, M. H. Dickinson, *J. Exp. Biol.* **1997**, *200*, 1133.
- [4] G. Bledt, M. J. Powell, B. Katz, J. Di Carlo, P. M. Wensing, S. Kim, presented at *IEEE Int. Conf. Intell. Robots Syst.* Madrid, Spain, October, **2018**.
- [5] K. Y. Ma, P. Chirarattananon, S. B. Fuller, R. J. Wood, *Science*. **2013**, *340*, 603.
- [6] X. Ji, X. Liu, V. Cacucciolo, M. Imboden, Y. Civet, A. El Haitami, S. Cantin, Y. Perriard, H. Shea, *Sci. Robot.* **2019**, *4*, eaaz6451.
- [7] Y. Wu, J. K. Yim, J. Liang, Z. Shao, M. Qi, J. Zhong, Z. Luo, X. Yan, M. Zhang, X. Wang, *Sci. Robot.* **2019**, *4*, eaax1594.
- [8] a) T. Fukuda, H. Hosokai, I. Kikuchi, presented at *IEEE ICRA*, Cincinnati, OH, May, **1990**;  
b) A. Villanueva, C. Smith, S. Priya, *Bioinspir. Biomim.* **2011**, *6*, 036004.
- [9] X. Huang, K. Kumar, M. K. Jawed, A. M. Nasab, Z. Ye, W. Shan, C. Majidi, *Sci. Robot.* **2018**, *3*, 7557.
- [10] a) N. W. Bartlett, M. T. Tolley, J. T. Overvelde, J. C. Weaver, B. Mosadegh, K. Bertoldi, G. M. Whitesides, R. J. Wood, *Science*. **2015**, *349*, 161; b) M. T. Tolley, R. F. Shepherd, M. Karpelson, N. W. Bartlett, K. C. Galloway, M. Wehner, R. Nunes, G. M. Whitesides, R. J. Wood, presented at *IEEE Int. Conf. Intell. Robots Syst.* Chicago, IL, September **2014**.

- [11] J. Liang, Y. Wu, J. K. Yim, H. Chen, Z. Miao, H. Liu, Y. Liu, Y. Liu, D. Wang, W. Qiu, *Sci. Robot.* **2021**, *6*, eabe7906.
- [12] H. Wang, P. York, Y. Chen, S. Russo, T. Ranzani, C. Walsh, R. J. Wood, *Int J Rob Res.* **2021**, *40*, 895.
- [13] R. Pelrine, R. D. Kornbluh, Q. Pei, S. Stanford, S. Oh, J. Eckerle, R. J. Full, M. A. Rosenthal, K. Meijer, presented at *Smart Mater. Struct.* **2002**.
- [14] E. Acome, S. K. Mitchell, T. Morrissey, M. Emmett, C. Benjamin, M. King, M. Radakovitz, C. Keplinger, *Science.* **2018**, *359*, 61.
- [15] M. Duduta, E. Hajiesmaili, H. Zhao, R. J. Wood, D. R. Clarke, *Proc. Natl. Acad. Sci. U. S. A.* **2019**, *116*, 2476.
- [16] a) F. Berlinger, M. Duduta, H. Gloria, D. Clarke, R. Nagpal, R. Wood, presented at *IEEE ICRA*, Brisbane, Australia, May **2018**; b) G. Li, X. Chen, F. Zhou, Y. Liang, Y. Xiao, X. Cao, Z. Zhang, M. Zhang, B. Wu, S. Yin, *Nature.* **2021**, *591*, 66.
- [17] Y. Chen, H. Zhao, J. Mao, P. Chirarattananon, E. F. Helbling, N.-s. P. Hyun, D. R. Clarke, R. J. Wood, *Nature.* **2019**, *575*, 324.
- [18] Y. Chen, S. Xu, Z. Ren, P. Chirarattananon, *IEEE Trans. Robot.* **2021**.
- [19] N. T. Jafferis, E. F. Helbling, M. Karpelson, R. J. Wood, *Nature.* **2019**, *570*, 491.
- [20] X. Yang, Y. Chen, L. Chang, A. A. Calderón, N. O. Pérez-Arancibia, *IEEE Robot. Autom. Lett.* **2019**, *4*, 4270.
- [21] J. James, V. Iyer, Y. Chukewad, S. Gollakota, S. B. Fuller, presented at *IEEE ICRA*, Brisbane, Australia, May **2018**.

- [22] D. S. Drew, N. O. Lambert, C. B. Schindler, K. S. Pister, *IEEE Robot. Autom. Lett.* **2018**, 3, 2807.
- [23] Y. Zou, W. Zhang, Z. Zhang, *IEEE Trans. Robot.* **2016**, 32, 1285.
- [24] M. Duduta, R. J. Wood, D. R. Clarke, *Adv. Mater.* **2016**, 28, 8058.
- [25] H. Zhao, A. M. Hussain, M. Duduta, D. M. Vogt, R. J. Wood, D. R. Clarke, *Adv. Funct. Mater.* **2018**, 28, 1804328.
- [26] E. Hajiesmaili, D. R. Clarke, *J. Appl. Phys.* **2021**, 129, 151102.
- [27] J. P. Whitney, R. J. Wood, *J. Fluid Mech.* **2010**, 660, 197.
- [28] S.P. Sane, M.H. Dickinson, *J. Exp. Bio.* **2002**, 205, 1087-1096.
- [29] N. Doshi, B. Goldberg, R. Sahai, N. Jafferis, D. Aukes, R.J. Wood, presented at *IEEE IROS*, Hamburg, Germany, September **2015**.
- [30] M. Graule, P. Chirarattananon, S. Fuller, N. Jafferis, K. Ma, M. Spenko, R. Kornbluh, R. Wood, *Science*. **2016**, 352, 978.
- [31] Y. M. Chukewad, S. Fuller, *IEEE Robot. Autom. Lett.* **2021**, 6, 1864.
- [32] K. Y. Ma, P. Chirarattananon, R. J. Wood, presented at *IEEE Int. Conf. Intell. Robots Syst.* Hamburg, Germany, September, **2015**.
- [33] S. B. Fuller, *IEEE Robot. Autom. Lett.* **2019**, 4, 570.
- [34] Y. Chen, K. Ma, R. J. Wood, presented at *IEEE Int. Conf. Intell. Robots Syst.*, Daejeon, South Korea, October, **2016**.

## Table of Contents text

This work presents a low voltage, long endurance, and power-dense dielectric elastomer actuator (DEA) based on novel multiple-layer fabrication methods and electrode material optimization. An insect-scale micro-aerial-vehicle (MAV) is designed with this DEA. The robot achieves the best performing and longest hovering flight among sub-gram MAVs. This type of DEA shows promise in making next-generation agile soft robots.

